

Complex fracture energy dissipation in concrete under different loading conditions

Alberto Carpinteri^{a,*}, Bernardino Chiaia^a, Kamran M. Nemati^{b,1}

^a *Department of Structural Engineering, Politecnico di Torino, Corso Duca d. Abruzzi 24, 10129 Turin, Italy*

^b *University of California at Berkeley, Department of Civil Engineering, 721 Davis Hall, Berkeley, CA 94720, USA*

Received 28 May 1996; received in revised form 31 March 1997

Abstract

Two different investigations on the scaling properties of damage in concrete have been carried out. In the case of uniaxial tensile tests, a laser profilometer was adopted to scan the post-mortem fracture surfaces. In the case of compression tests, a fusible alloy (Wood's metal) was injected inside the specimen under load (ante-mortem). Afterwards, scanning electron microscope was used on the sliced specimens to detect the stress-induced crack patterns. The highly localized energy dissipation in uniaxial tension evolves from a narrow damage band to a fracture surface with fractal dimension comprised between 2.0 and 2.5. The microcracks networks induced by compression present fractal dimension even larger than 2.5 in the bulk. Fractality permits to explain some aspects of the fracture behavior, like the stable crack growth encountered in the tests and the smoothing of the dynamic stress-intensity factor which causes the cracks to propagate slower than at the theoretical Raleigh speed. © 1997 Elsevier Science Ltd.

Keywords: Concrete; Microcracking; Fractography; Fracture energy; Disorder; Fractality

1. Introduction

1.1. Tensile failure in concrete

Concrete is a heterogeneous material that exhibits strain-softening behavior and fails progressively by damage-localization and breakdown of its components. Moreover, it is characterized by considerable size-effects and by a marked difficulty in the reproducibility of the tests. Brittle fracture in concrete

structures represents a typical example of cusp catastrophe (Carpinteri, 1989). According to this concept, the system of dissipative processes (microcracking, creep, plasticity) can transfer to a thermodynamic equilibrium state only by a jump, as a result of a critical phase transition at a bifurcation point. If a tensile load is increased beyond the peak (load-controlled process), the complete fracture of the specimen occurs. If a displacement-controlled process is carried out, the softening regime comes into play, which is clearly unstable in the sense of Drucker. The continuum mechanics approach fails to predict these aspects, and also linear elastic fracture mechanics (LEFM) is inadequate because of the scale of heterogeneities.

* Corresponding author. Tel.: +39-11-5644850; fax: +39-11-5644899; e-mail: carpinteri@polito.it.

¹ E-mail: nemati@nemati.com.

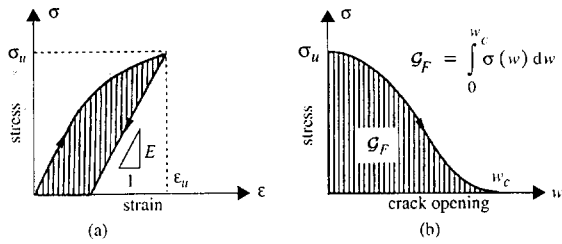


Fig. 1. Cohesive crack model (Hillerborg et al., 1976).

Since the pioneering works of Griffith, energy-based failure criteria proved to be more appropriate than stress criteria to describe tensile failure of brittle materials. Afterwards, LEFM has been extrapolated and nonlinear models have been introduced to explain peculiar phenomena occurring in the presence of meso-level heterogeneities. The constitutive model that best describes the tensile behavior of concrete is the Cohesive Crack Model by Hillerborg et al. (1976), which is based on two different relationships. The first one (Fig. 1a) is the elastic–plastic *stress–strain* law, holding up to the ultimate tensile stress σ_u , and the second one (Fig. 1b) is a *stress–crack opening displacement* law, also called the *cohesive law*, which describes the softening behavior provided by the damaged process zone.

The area under the cohesive law $\sigma(w)$ represents the energy dissipated on the unitary crack surface and, by definition, is called the *fracture energy* \mathcal{G}_F of the material. The cohesive law is assumed as a material characteristic, since it intimately depends on the microstructure and on the dissipation mechanisms involved in the fracture process (bridging, creep, aggregate interlocking). Therefore, the fracture energy \mathcal{G}_F is usually assumed as a material constant.

According to its definition, the fracture energy \mathcal{G}_F does not represent a *local* toughness parameter, like the critical stress–intensity factor K_{IC} (*tensile fracture toughness*). It rather represents a *mean-field* quantity, involving the whole complexity of microscopical phenomena ahead of the crack tip, which contribute to the *total* work-of-fracture (*energy fracture toughness*). The great advantage of such a global parameter is provided by the absence of linearity requirements in the fracture process. No information on the singular stress field at the crack tip is needed,

and LEFM can be neglected. On the other hand, the physical meaning of \mathcal{G}_F is ambiguous. \mathcal{G}_F is considered to be dissipated on the nominal (smooth) area of the final separation surface and therefore is defined as surface energy ($[F][L]^{-1}$). On the contrary, it refers to a much more complex process of dissipation, occurring in a *higher dimensional fractal domain* (Carpinteri and Chiaia, 1995a), where several micromechanisms of damage take place and interact at various scales.

1.2. Compressive failure in concrete

The composite nature of concrete represents the major difficulty in developing a fracture criterion for concrete in compression. It is nowadays clear that a sound explanation of the behaviors observed in the laboratory and in real-sized structures can be obtained only if the complex microcracking phenomenon is taken into account (Vonk, 1993). Similar crack patterns in similar uniaxial compressive tests have been detected, at different scales, in different materials like glass, concrete, rocks and masonry. The similarity in the cracking behavior of different brittle materials emphasizes common fundamental fracture mechanisms.

The dominant mechanism of brittle fracture in compression is basically Mode I cracking, the same as in tension. Nemat-Nasser and Hori (1993) successfully explained how, even under all-around compressive loads, brittle materials tend to fail by the formation of tensile microcracks at microdefects such as cavities, inclusions and grain interfaces. Tensile stresses break interatomic bonds and pour the surfaces apart. Nevertheless, a completely different behavior is provided by the overall tensile strains, which are parallel to the load direction in the case of tensile tests, and mainly perpendicular to the load direction in the case of uniaxial or biaxial compression tests. Whilst, in the former case, the overall tensile strains are limited (to about 10^{-4}) because microcrack propagation is highly unstable, in the latter case the overall tensile strains can be ten times greater.

However, this does not totally exclude Mode II or Mode III cracking, or their combination, but it is believed that these Modes come into play in the last stages of the failure process, whilst in the pre-peak

regime they may occur only at a local scale as second-order effects. Macroscopic failure modes frequently observed in compression tests, such as conical, pyramidal or wedge-shaped modes, are mainly due to the boundary confinement of the loading platens. Under the usual testing conditions, the stress field in the specimen is highly anisotropic and not uniaxial at all. The so-called shear failure is nowadays considered a secondary (macro) effect which occurs after the axial splitting has begun. Shear bands and shear displacements are not fundamental mechanisms of failure, but only the consequence of boundary restraint.

In uniaxial compressive tests, macroscopic cracks essentially start parallel to the direction of axial loading. Experimental as well as theoretical explanations for this behavior in *heterogeneous* materials are nowadays well established (Nemat-Nasser and Hori, 1993). Instead, convincing theoretical explanations are lacking for the propagation of a parallel crack during a uniaxial test in a *homogeneous* material. Stress-based criteria would request the presence of tensile stresses. Further, energy-based criteria fail if no source of energy release is present, as it is the case of a hairline crack parallel to the direction of load, which apparently alters neither the strain energy nor the total potential energy. The only reliable explanation for this behavior is provided by the intrinsic heterogeneity of the material, and especially by the presence of cracks, pores and voids even prior to the application of the load. Griffith postulated that brittle materials contain randomly oriented flaws which significantly alter stress-strain fields in the bulk. As well as pre-existing flaws act as stress-raisers in tensile tests, they can be considered tensile stress producers in compression. Indeed, the presence of voids in concrete strongly reduces its strength. That is, 5% of voids can lower compressive strength by as much as 30% compared to the same mixture when fully compacted.

Any constitutive or geometrical heterogeneity alters the stress-strain field, and thus may promote crack initiation. On the other hand, heterogeneity may also stop or slow down crack propagation. This duality represents an awkward aspect to be modelled. It can be concluded that the interplay between the tensile stress-inducing capacity and the crack-arresting capacity of the micro-heterogeneities is the key

for a better understanding of brittle failure in compression.

2. Fractal models of heterogeneous microstructures

The characteristic features of critical phenomena, such as hierarchy of interacting defects, stochasticity and far-from equilibrium instabilities, are present in both tensile and compressive failure modes. The irregularity of the crack trajectories is a well documented and discussed phenomenon. The two potential sources of disordered damage patterns are the intrinsic instability of the cracking process and the effect of the (random) pre-existing material inhomogeneities. An extensive documentation exists on the stability of crack trajectories to small perturbations and it is nowadays widely demonstrated that the quenched disorder of brittle fracture patterns cannot be ascribed to crack-tip instabilities. It can be concluded that *the main source of randomness and chaotic behavior is the inherent disorder of the material microstructure*. Whenever *entropy wins over energy*, the resulting structure will be dominated more by randomness than by strict Euclidean order and we might expect to find fractal patterns with self-similar scaling symmetry (Mandelbrot, 1982).

The application of Fractal Geometry to cementitious materials is relatively recent in comparison with the application to rocks and metals, but has proven to be very appropriate, due to the *multi-scale heterogeneity* of these materials (Carpinteri, 1994). This is reflected into the *hierarchical process of failure*. The interfacial zone between cement paste and aggregates is one of the weakest areas of the concrete microstructure. Cracks usually originate from pre-existing flaws (pores) in the matrix and at the interfaces (micro-level). Afterwards, they develop at the scale of the matrix (meso-level), and finally extend to the structural scale (macro-level), resulting in a typically disordered pattern with multiple cracking randomly diffused at the interfaces, through the matrix and through the aggregates. It can be noticed that this propagation process leads to more organized patterns at larger scales.

The main aspect to be highlighted, next to the phenomenological evidence, is the physical signifi-

cance of fractality. In the framework of critical phenomena a deep connection has been established between Physics and Topology. All the physical systems undergoing catastrophic transformations, like phase transitions, earthquakes and brittle fracture, show at the critical point fluctuations that are *self-similar* at all length scales, thus resulting in the (theoretical) absence of any internal characteristic length (or, which is the same, in the *infinite correlation length* of the phenomenon).

In the case of fracture patterns, *invasive fractals* (i.e., fractal sets with dimension Δ strictly larger than their euclidean projection) represent adequate models of their topology. The *random von Koch curve* (Fig. 2a) can be considered the archetype of the fracture trajectories obtained as intersections of tension-generated fracture surfaces with orthogonal planes. The Peano curve (Fig. 2b) represents the limiting invasive fractal in the plane (fractal dimension $\Delta = 2$), because establishes a continuous correspondence between the straight line and the plane. The space-filling ability of these sets provides *positive scaling exponents* for the mechanical quantities (e.g., the fracture energy) defined over them (Carpinteri, 1994).

All the fractal sets in Nature show *random* self-similar morphologies, in the sense that their aspect

looks *statistically* (and not exactly, as in the case of mathematical fractals) the same under the changes in the scale of observation. Besides randomness, two more aspects have to be enlightened that are peculiar for all the natural fractal structures. First of all, the presence of an upper and a lower bound in the scaling range and, consequently, the inevitable transition occurring from the fractal (disordered) regime at the microscopic level towards an euclidean (homogeneous) regime at the largest scales. The upper bound is represented by the macroscopic size of the set, whilst the lower one is related to the size of the smallest measurable particles, these being the grains, in the case of metals, the crystals, in the case of rocks, and the aggregates, in the case of concrete. It can be argued that the presence of this *internal length*, typical of each microstructure, inhibits the development of a perfect self-similar scaling through the whole scale range, whereas mathematical fractals (Fig. 2), lacking any characteristic length, exhibit uniform (monofractal) scaling without any bound and can be characterized by a unique value of the self-similarity dimension.

Mandelbrot (1985) pointed out the transition from a fractal regime, characterized by the so-called *local* fractal dimension, to the homogeneous one, characterized by the classical (integer) topological dimen-

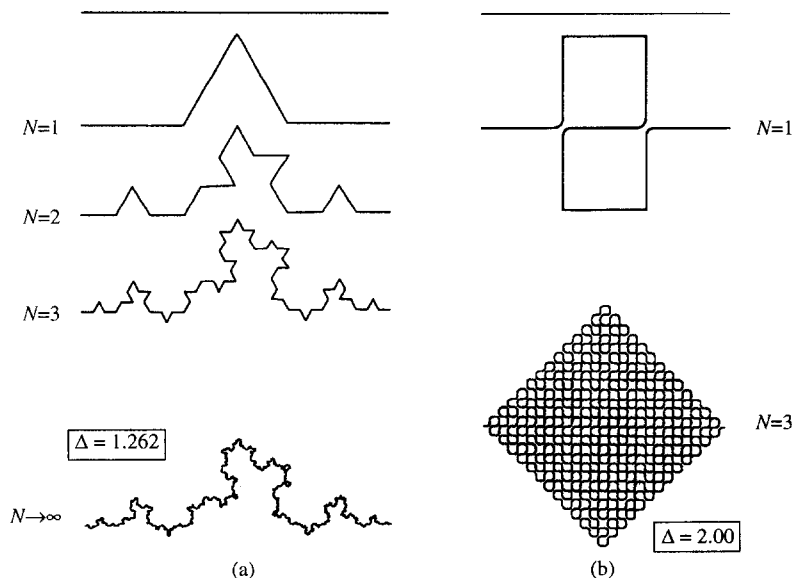


Fig. 2. Invasive fractals: random von Koch curve (a) and Peano curve (b).

sions. Such non uniform scaling can be defined as 'self-affinity'. One step forward is *geometrical multifractality* (Carpinteri and Chiaia, 1995a). The two regimes are considered only the asymptotics of a continuous topological transition. Therefore, an infinity of exponents is necessary to describe the entire range of the scaling. Multifractal patterns prevail in Nature whenever the interplay between two length scales occurs.

3. Experimental investigation on the fractality of tensile fracture surfaces

3.1. Experimental set-up

Bone-shaped concrete specimens have been tested in uniaxial tension and the resulting fracture surfaces have been subsequently analyzed. A laser displacement sensor (3 mW semiconductor, class IIIb) has been used to scan the surfaces along parallel profiles. The wavelength of the laser beam was 780 nm, allowing for an accuracy of $\pm 2 \mu\text{m}$. This yields a significant improvement with respect to previous investigations (Carpinteri and Chiaia, 1995a) and represents, for our purposes, the optimal resolution in the case of cement-based materials. For an optimal measurement set-up, the sensitivity of the laser was adjusted to fit the optical properties of the concrete surface (color, light absorption and reflection, and so on).

The laser sensor was mounted on an advanced motion controller system, at a distance of approximately 25 mm from the concrete surface (Fig. 3).

The mechanical system shifts the sensor along two perpendicular directions (x and y coordinates), usually parallel to the main sides of the cross section, with horizontal steps equal to 0.01 mm. After each step, the guide stops and the profile elevation (z coordinate) is detected by the sensor and stored in the computer along with the horizontal coordinates. Due to inertial forces, a $\pm 1 \mu\text{m}$ error is present in the determination of the horizontal coordinates.

In principle, given the coordinates of a limited area on the surface, the procedure is fully automated, and a 3D topography of the fracture surface is obtained. On the other hand, a $10 \times 10 \text{ cm}^2$ area (which is the minimum representative area for a normal concrete) consists of about 100 million digitized points, that is, 300 million stored coordinates. This results in an enormous computational effort when the fractal dimension has to be measured on standard computers. Thus it was decided, in a first stage, to analyze single profiles (2D topography). Six profiles have been digitized on each specimen, three along each perpendicular direction, in order to average out the effects of highly correlated directions of propagation.

3.2. Determination of the fractal dimension of fracture profiles

Deterministic and stochastic methods can be exploited for the measurement of the fractal dimension of fracture patterns. In principle, they are all equivalent in the limit of the smallest scales, but they differ significantly when applied to digitized profiles. Most of the methods (e.g., the Divider method and the

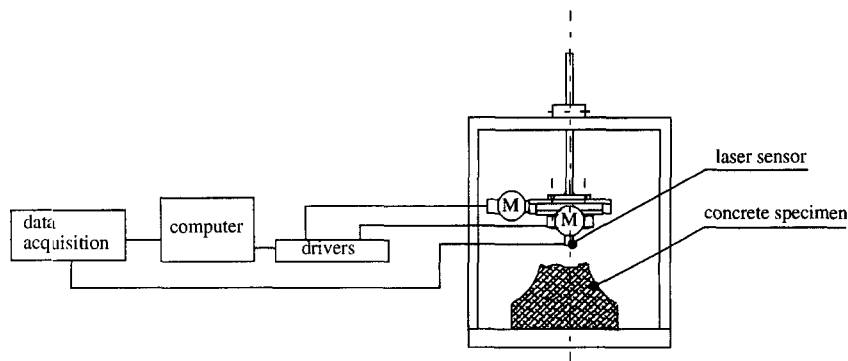


Fig. 3. Laser-digitization of fracture profiles: scheme of the experimental set-up.

Spectral method) are tailored to the case of one variable function graphs. Moreover, the Spectral method is rigorously demonstrated only in the case of self-affine scaling. Thus, it was decided to adopt the 2D box-counting method which, on the contrary, applies to any (invasive or lacunar) fractal domain referred to the 2D plane. Both the tensile fracture profiles and the compressive crack networks can be analyzed by this method.

The box-counting method is based on the concept of the Minkowski–Bouligand dimension. The *Minkowski-cover* of a set is obtained by covering the considered domain by means of a collection of regular euclidean figures, with dimension equal to the space in which the fractal is embedded. The fractal dimension is obtained by computing the *logarithmic density* of the measure of these coverings, as their linear size decreases. In principle, the concept of *generalized cover* allows one to adopt any kind of convex shapes to perform the covering. On the other hand, from a computational point of view, square or rectangular grids are always used. In order to study the complex patterns resulting from the experimental tests, a general-purpose version of the method has been developed. As the linear size ϵ of the covering boxes decreases, their number N increases and their area E decreases (Fig. 4). The box-dimension Δ is given by:

$$\Delta = \lim_{\epsilon_i \rightarrow 0} \left(\frac{\log N(\epsilon_i)}{\log(1/\epsilon_i)} \right) = 2 - \lim_{\epsilon_i \rightarrow 0} \left(\frac{\log |E(\epsilon_i)|_2}{\log \epsilon_i} \right). \quad (1)$$

In practical applications, instead of dealing with a limit, *linear regression* is carried out in the $\log N$

vs. $\log \epsilon$ plot or in the $\log E$ vs. $\log \epsilon$ plot. The slopes φ and ϑ are respectively obtained and the Box-dimension is computed as $\Delta = -\varphi$ or as $\Delta = 2 - \vartheta$. Further details on the algorithm have been explained by Carpinteri and Chiaia (1995a).

The fracture process under uniaxial tension is highly unstable. After an initial stage of randomly distributed microcracking (usually at the interface between aggregates and matrix) correlations between the cracks increase and a well-defined band is selected for the main dissipation. The interface microcracks and the pre-existing pores become attractors of the macrocrack propagation. It has been demonstrated (Vervuurt et al., 1995) that these networks are self-similar. The fractal dimension of the networks can exceed 1.5 in the 2D projection. Complex interactions among microcracks occur at this stage. Self-organized dissipation increases ductility, macroscopically providing the softening regime of the load-deformation curve.

When the final breaking of the specimen occurs (catastrophic transition), a single self-affine fracture surface is generated whose local dimension is bounded by 2.5 (Brownian surface). Therefore, in the case of fracture profiles, direction-dependent rescaling of the grid has to be performed, because of the self-affine character of the set. Instead of considering only the local fractal dimension at microscales and the topological dimension at large scales, the entire scaling range is swept by the box-counting algorithm. Anisotropic grids are used, in order to enhance the statistical fluctuations in one direction. In this way, it is possible to detect the *local* fractal dimension in the limit of the smallest grids (Fig. 5).

The multifractal character of the fracture profiles

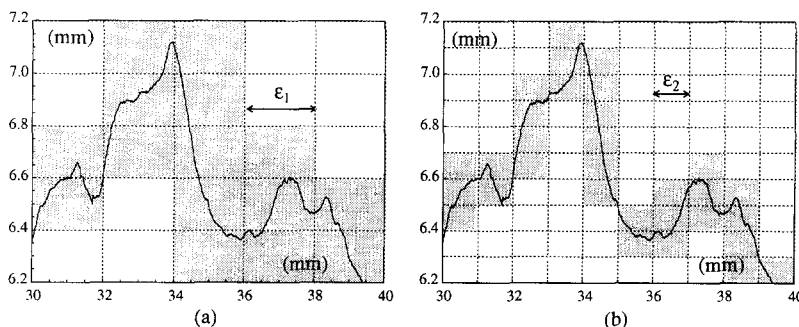


Fig. 4. Application of the box-counting method to a digitized concrete profile.

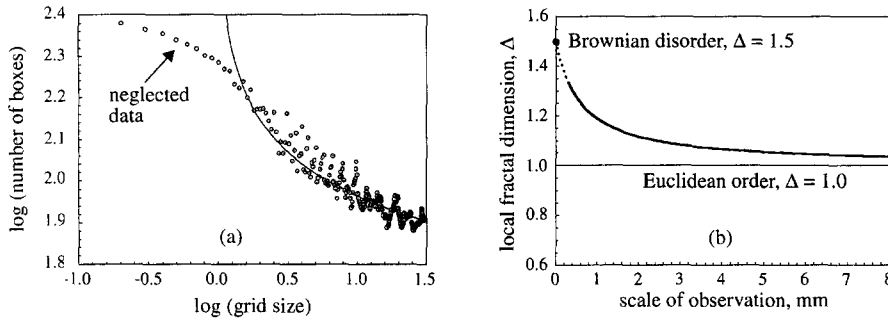


Fig. 5. Double-logarithmic plot from the box-counting method (a), and multifractal transition from Euclidean order to Brownian disorder (b).

clearly emerges from the box-counting analysis. Multifractal scaling is provided, in fact, by the interplay between the (mainly horizontal) crack advancement and the orthogonal direction. Not a unique slope can be traced in the double-log diagram (Fig. 5a), but the fractal dimension Δ progressively decreases as the scale of observation increases. The densifying ability of the domain vanishes at coarse scales (macro-level), where a smooth euclidean profile is measured. On the contrary, as the grid size

tends to zero (micro-level), the fractal dimension increases, ideally tending to 1.5 which is the local fractal dimension of a unidimensional Brownian motion in the space vs. time domain (Fig. 5b). This trend, already captured by previous investigations (Carpinteri and Chiaia, 1995a), is even more pronounced due to the higher resolution in the data acquisition. Local dimensions Δ_1 ranging from 1.28 to 1.42 were measured at the smallest scales, testifying the tendency to 1.5. Extrapolating from the pro-

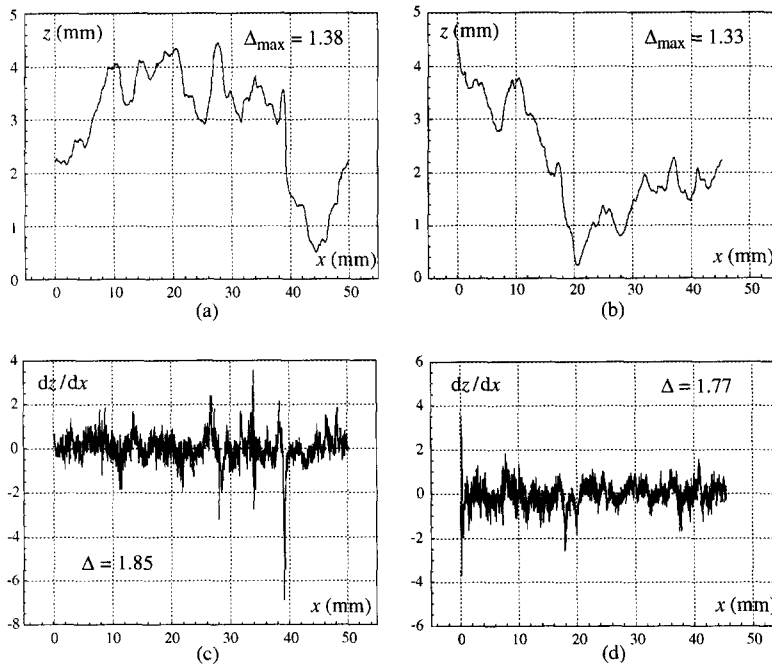


Fig. 6. Profile elevations (a, b) and plot of the increments (c, d) for two profiles.

files to the surfaces, a limiting dimension equal to 2.5 should be attained.

It is worth pointing out that discreteness effects come into play when the grid size is close to the digitization step (i.e., 10 μm). Therefore, data in the upper left side of the double-log diagram have to be neglected (Fig. 5a). This represents an unavoidable drawback of *any* experimental measure of fractality on real sets, regardless of the data-acquisition method and of the measurement algorithm. Discreteness effects arise also in the case of SEM images of compression-induced crack networks, strongly affecting the image analysis procedure (Fig. 9f).

Confirmation of the Brownian character of the fracture surfaces comes from the analysis of the *elevations growth rate* (derivative) of the profiles. In the ideal case of geometrical Brownian motion, the plot of the increments possesses Hausdorff dimension equal to 2.0 and its power spectrum is absolutely flat (Mandelbrot, 1982). No correlation is present between two subsequent increments and self-similar scaling comes into play (Gaussian white noise), meaning that the system of the increments lacks any characteristic scale.

The trail of the Brownian motion can be intended as the integral of a white noise and possesses fractal dimension equal to 1.5. Self-affine scaling is provided in this case, and an internal length characterizes the graph. In fact, if we rescale the horizontal axis by a factor b and the vertical axis by a factor $b^{1/2}$, we reproduce the original distribution of the motion. Short-range correlations are present in the graph, as well as long-range ones. Indeed, short-range correlations prevail, meaning that the position of each point in the graph is dependent on the position of all the other points, but mainly on the position of the surrounding ones. Therefore, the power spectrum ($S(f) \approx f^{-2}$) steeply decreases as the spatial frequency increases.

In the case of concrete fracture profiles, analysis of the growth rates (Fig. 6c, d) yields fractal dimensions ranging from 1.71 to 1.94. This confirms the hypothesis of Brownian disorder underlying the fracture phenomenon. This assumption, although not yet proved by experiments, is suggestively supported by Chudnowski and Kunin (1987), who demonstrated that Brownian surfaces arise as the result of the interplay of randomness and optimality. In the case

of fracture, randomness is present in the distribution of material properties and therefore in the micro-cracks nucleation, whereas optimality is obviously related to the energy expenditure during formation of the fracture surface.

Recent applications of these concepts to turbulence (El Naschie, 1996) lead also to affirm that a connection must exist between all the chaotic dissipative phenomena. Extrapolation of the results to 3D sets is straightforward, since 2D profiles can be considered intersections of the 3D surface with vertical planes. Indeed, 3D correlations cannot be revealed by the profile analysis. It can be concluded that the box-dimensions measured on 2D profiles represent a lower bound of fractality in concrete tensile fracture surfaces.

4. Experimental investigation on the fractality of compression-induced damage patterns

4.1. Experimental set-up and specimen preparation

Wood's metal porosimetry techniques were pioneeringly applied by N. Cook and his co-workers at the Berkeley Labs (Zheng et al., 1988). This non-destructive technique allowed to investigate deeply in the micro-mechanisms involved in the whole mechanical behavior of rocks under compression loading (Myer et al., 1992), giving experimental validation to the theoretical models proposed by Nemat-Nasser and Hori (1993). The technique, essentially, makes it possible to preserve the compressive stress-induced microcracks in porous materials as they exist under applied loads. In this section, the application of this technique to concrete is illustrated (Nemati, 1994). The results of these experiments have been used to better understand and quantify the general relationship between stress level and crack development, as well as the effects of confinement on crack behavior. A special test equipment was created to preserve the cracks under applied load. This was accomplished by injecting a molten metal into the induced cracks and solidifying it before unloading. The experiments carried out involved three procedures, namely the concrete casting and preparation, the crack induction, and the molten

metal injection and solidification. The second and third procedures were carried out simultaneously.

Normal-strength concrete cylinders, 203 mm long by 102 mm in diameter, were cast using a standard mix design at the Civil Engineering Materials Laboratory of the University of California at Berkeley. The compressive strength of the samples was approximately 51.7 MPa. Wood's metal, whose commercial name is Cerrosafe™, is a fusible alloy. In the liquid phase it is non-wetting, with an effective surface tension of about 400 mN/m. It consists of 42.5% bismuth (Bi), 37.7% lead (Pb), 11.3% tin (Sn), and 8.5% cadmium (Cd). It has a melting point range from 71.1°C to 87.8°C, and is solid at room temperature. Wood's metal has a Young's modulus of 9.7 GPa and a density of 9.4 g/cm³. The advantage of such an alloy is that it can be injected into voids and stress-induced microcracks at the desired stress level, then solidified during the experiment to preserve the geometry of the induced microcracks at any given stage of the experiment (Zheng et al., 1988).

The equipment used for this research was specially designed and developed at the University of California at Berkeley. It consists of five pieces: pedestal, vessel, piston, top cap, and heater (for description and detailed design of the test equipment refer to Nemati, 1994). Two different loading conditions, uniaxial and triaxial, were used to induce cracks in the concrete cylinders. Triaxiality was provided by the wire wound around the concrete cylin-

ders. After preparation for testing, each concrete cylinder was first dried in an oven at a temperature of 43.3°C. This removed the moisture in the concrete and preheated the cylinder, ensuring that the molten metal alloy could penetrate into pores and cracks deep within its core without solidifying prematurely. The concrete cylinder was then placed on the pedestal inside the vessel and the piston was placed on top of it. A LVDT (linear variable displacement transducer) for the axial displacement measurement was attached to the loading frame. Wood's metal was poured into the vessel and once the concrete cylinder was submerged in the molten metal the top cap was closed and then bolted tightly to the vessel. Fig. 7 shows a schematic diagram of the test assembly. To monitor the temperature, a thermocouple was inserted into a predrilled hole on the top cap. The heater was then placed around the assembled system with a special noncombustible board placed on top to prevent heat convection and thus uniform heating of the test assembly.

The heat was supplied in three stages. Starting at room temperature, the heat was ramped up to 50°C and held at that temperature for 10 min. Then the temperature was ramped up to 75°C and held there for an additional 10 min. The final stage involved ramping the temperature up to a target of 96°C for a period of 15 min and holding it at that temperature until the heat was no longer needed. The ceramic heater was placed around the vessel to liquefy the Wood's metal inside and to maintain a constant

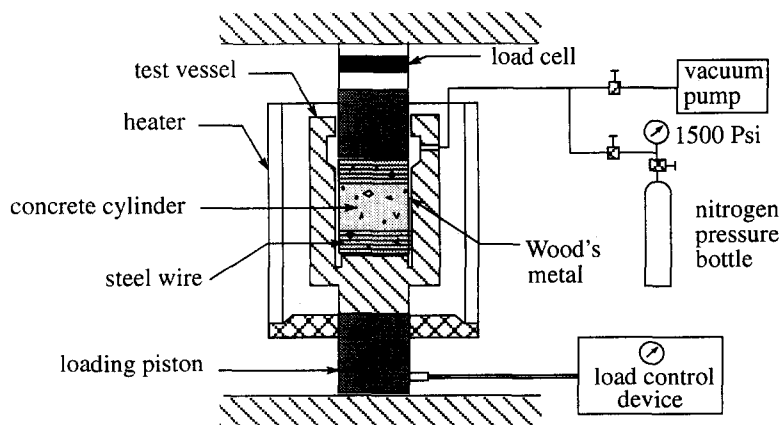


Fig. 7. Schematic diagram of test assembly in the case of compression tests.

temperature throughout the experiment. This temperature was, in turn, monitored by a thermocouple that was attached to the side of the top cap.

With the internal temperature thus established and maintained at 96°C, vacuum was applied to the vessel and kept constant for at least 30 min. The vacuum removed any air that had become trapped in the concrete cylinder when it was assembled inside the vessel. An axial stress of up to 90% of the ultimate strength was applied to the concrete cylinder, at which point the vacuum was removed. Finally, in order to saturate the induced microcracks with the molten metal, nitrogen pressure was applied to the top of the vessel. It was controlled by a high-pressure regulator on a bottle of nitrogen. A nitrogen pressure of 10.3 MPa was applied to the molten metal as the pore pressure, which was kept constant throughout the tests and which did not alter the effective stresses on the concrete cylinder. With a surface tension of 400 mN/m, the alloy could penetrate into flat cracks with apertures as fine as 0.08 μm .

Throughout the period of loading and unloading, the axial load and axial displacement were recorded on a data acquisition system and monitored on an X–Y plotter. The axial stress of interest was kept constant for 2 h to allow the liquid metal to penetrate into pores and fractures. Afterwards, fans were used to cool the vessel down to room temperature and to expedite solidification. Approximately 3 h elapsed between the time pore pressure was applied and the period during which the metal was allowed to solidify.

After each experiment, the concrete cylinder was sectioned along its long axis, using oil to cool the cutting saw. An axial slab, approximately 5 mm thick, was sliced parallel to the direction of the load. Four specimens were extracted from the axial slab. The next step was to polish the specimens for the SEM study. The concrete specimens extracted from the axial and lateral slabs were 25 mm square and had an approximate thickness of 5 mm. First, one side of each specimen was polished with 120#, 220#, 320#, and 600# silicon carbide using a rotating grinder and mounting it against a 25.4 mm diameter glass plate with epoxy. In order to make both sides of the specimen parallel to each other, the samples were cut 2–3 mm thick by using a diamond

slicing wheel with a nonaqueous lubricant (propylene glycol coolant). The specimens were then lapped with a wheel grinder and polished with 600# silicon carbide. Further polishing was performed with 100, 50, and 10 μm aluminum powder on a glass plate. The final stage involved treating specimens with 5, 3, and $\frac{1}{4}$ μm diamond paste using a special polishing equipment. After each stage of polishing, the specimens were immersed in acetone and placed in an ultrasonic machine in order to remove the residual silica film on their surfaces, thus preparing them for the next stage of polishing.

4.2. SEM image analysis and crack identification

After all the specimens were thus prepared, and prior to observation by SEM, they were gold coated. The single most important reason for coating or increasing the bulk conductivity is to increase the electrical conductivity of the sample. Materials of high resistivity, such as concrete, charge rapidly under the incident beam and might develop a potential sufficient to cause a dielectric breakdown in regions of the specimen. This could lead to variations in the surface potentials, giving rise to the complex and dynamic image artifacts commonly referred to as ‘charging’. A suitable conducting path may be established with a thin coating layer of gold which eliminates the problems associated with charging. Once the gold coat is in place, the specimen is then ready to be put into the scanning electron microscope (SEM).

After the concrete samples were prepared for scanning electron microscope studies, images were extracted from each sample. A total of four samples taken from the center and edge of the concrete cylinders in axial direction were studied. They were examined using a JEOL JSM-35CF scanning electron microscopy (SEM) with backscattered electrons (BSE) in conjunction with a KONTRON SEM-IPS image analyzer. For further details on the SEM technique, refer to Scrivener and Nematì (1996). The images were acquired by the image analyzer at magnifications of $\times 100$, $\times 1000$, $\times 10000$, $\times 20000$, and $\times 30000$. The images were digitized into an array of 512×512 pixels with 255 gray levels. SEM produces a multiphase image from each observation. In order to recognize and isolate Wood’s metal,

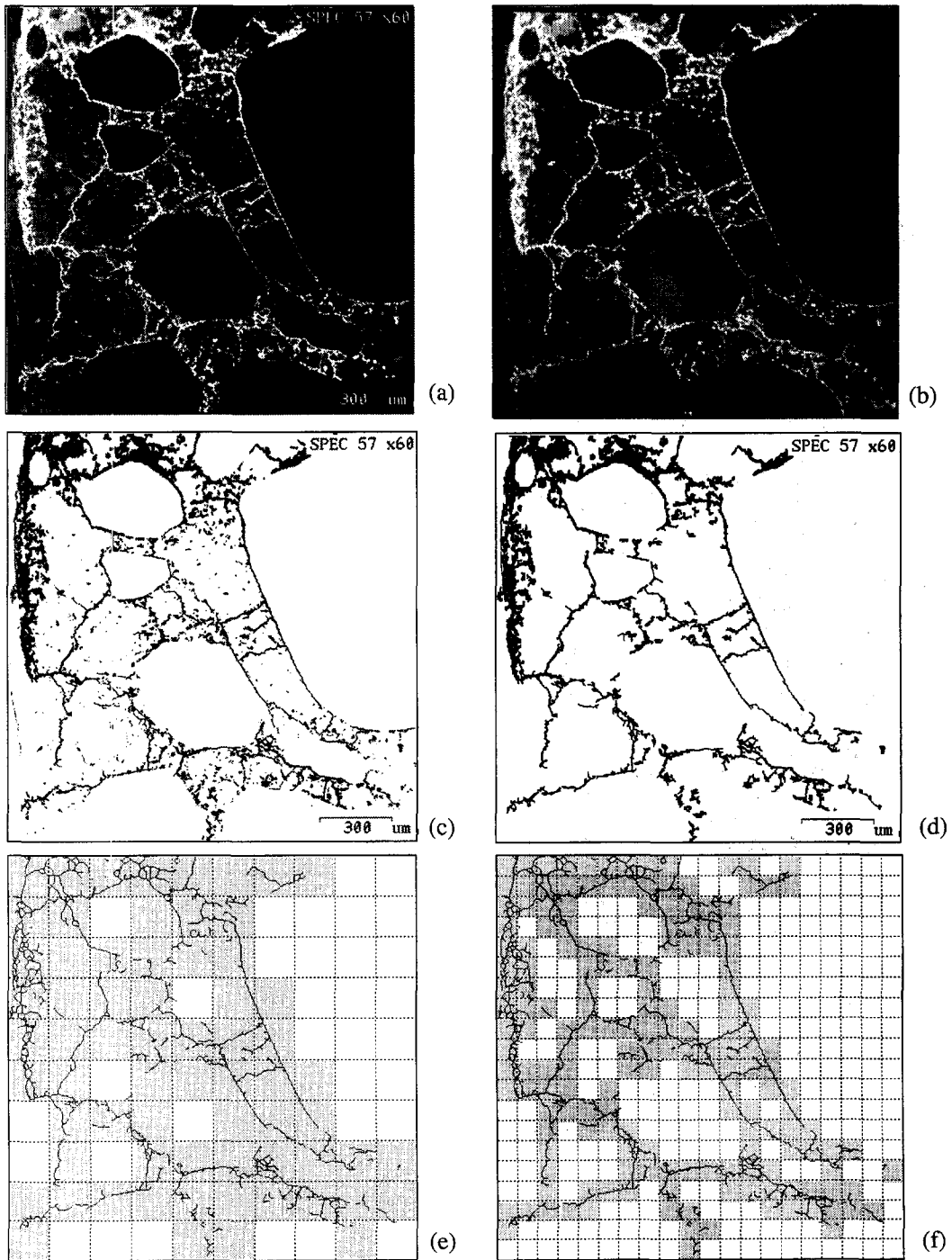


Fig. 8. SEM image of a crack network (a), histogram of grey levels (b), thresholded Wood's metal (c), and scrapping the pores (d). Application of the box-counting method to the thinned crack network (e, f).

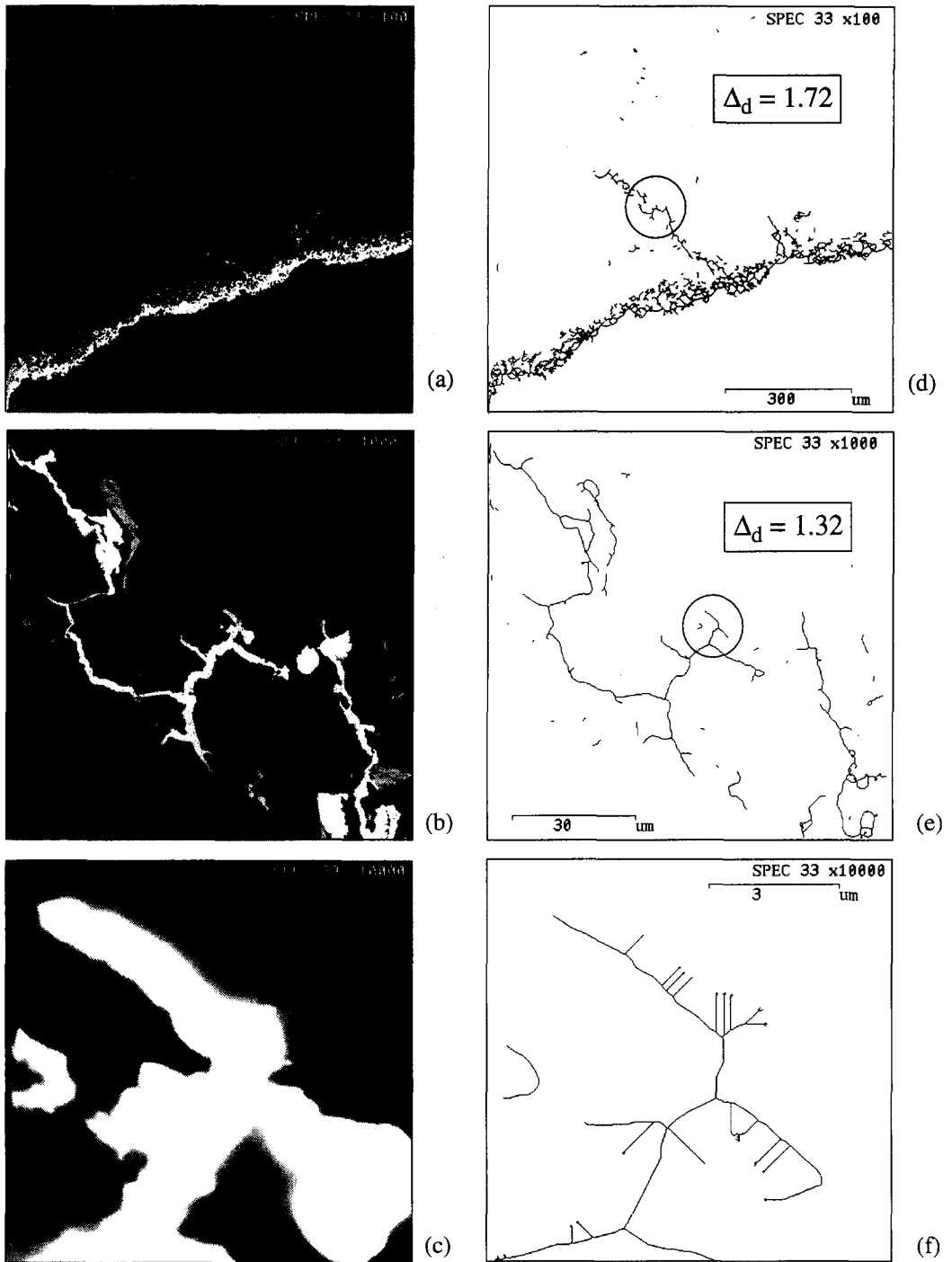


Fig. 9. Compression-induced crack networks with different SEM resolutions.

which is the representative of pores and fractures in concrete, the image analyzer can make a histogram for all of the different phases in the image based on their gray levels, with zero representing the darkest phase and 255 representing the brightest phase (Fig. 8a). From this histogram, and by means of the trial and error method, two threshold levels can be established to encompass the brightest phase in the image, namely Wood's metal. The threshold for Wood's metal identification was set between 170 and 255 (Fig. 8b). The next step is to eliminate objects from the background that do not fall between these threshold levels, i.e., cementitious phases and aggregates. Once the above task is accomplished, what is left in the image is the crack network and pores shown by Wood's metal (Fig. 8c).

At this point the aim is to eliminate objects on the basis of their area in pixel units. The lower and upper limits of the objects to be eliminated has to be established to include small pores, small non-continuous cracks, etc. (Fig. 8d). This procedure is called 'scrapping'. The next step is to transform this image into a skeletonized binary image by means of a binary thinning process. For every thinning step, pixels that are not relevant to the connectivity of an object are removed from the object margins, i.e., converted into background pixels. The connectivity of objects is thus maintained. This process can be continued until all objects are reduced to a width of one pixel that approximates the skeletons. The binary image in Fig. 8e represents the compressive stress-induced crack network in concrete as they exist under applied loads. Fig. 8e is the final binary image used for fractal measurements.

4.3. Determination of the fractal dimension of the crack networks

The application of the box-counting method to compression-generated damage patterns is different from that on the tensile fracture profiles. Because the crack advancement direction is highly inclined and curved, the orthotropy directions continuously change. Moreover, the high resolution of the SEM introduces a finer cut-off in the scaling behavior (about two orders of magnitude finer than in the case of the tensile profiles). Thus, SEM allows for the detection of crack branching and secondary cracks,

whereas the post-mortem digitization of the tensile fracture surfaces yields a series of fracture profiles which can be interpreted as one-variable function graphs. In the case of compression crack networks like those in Fig. 8, it seems more convenient to use isotropic square coverings, because damage at that scale is self-similar rather than self-affine.

Comparison between tensile fracture profiles and compressive patterns has to be made with care. Since the local mechanism of failure is Mode I cracking, the same as in tension (Nemat-Nasser and Hori, 1993), the local dimension of a single propagating crack should follow the same multifractal trend of tensile cracks. That is, a Brownian process should be reached in the limit of the microscales. Indeed, it is not straightforward to measure the *local* fractal dimension of a single crack on the thinned images. Instead, very interesting results come from the fractal analysis of the *global damage patterns* inside the specimen, which are directly related to the total dissipated energy W_F . The fractal dimension of the crack networks obtained thresholding the Wood's metal from the surrounding bulk can be called the *damage or network dimension* Δ_d (Fig. 8e and 8f). It must be clarified here that the damage dimension Δ_d maintains a deeply different significance with respect to the local dimension Δ of a single crack. Whilst Δ refers only to the local process of propagation, which is fractal because represents the optimal sequence of random micro-failures events, Δ_d reflects the self-organization of damage in a wide zone of material. As a consequence, self-organized dissipation increases ductility and may even promote crack arrest. Thus, it can be considered as a synthetic and *quantitative* measure of the complexity associated to the scale-invariant patterns of micro-fracture. A similar fractal description has been implemented for modelling the microcracks network induced in the proximity of the crack tip by tensile-splitting forces on notched concrete specimen (Vervuurt et al., 1995). The remarkable similarity of the damage patterns in these two cases confirms the relevance of local tensile ruptures under compressive loads.

An opposite trend with respect to the tensile fracture profiles is obtained when looking at the compressive damage patterns with increasing SEM resolution (Fig. 9). Chaotic self-similar patterns, resembling 2D diffusion fronts in porous media, are

revealed in the low-resolution images (0.304 pixels/ μm^2 , which is comparable to the laser resolution). High values of the damage dimension are measured at this scale (Fig. 9a, d), ranging from 1.65 to 1.79. A plane-filling network would possess fractal dimension Δ_d equal to 2.0, as in the case of the Peano curve (Fig. 2b). Extrapolating to 3D domains, this would yield a space-filling domain of microcracks, thereby implying a purely volumetric energy dissipation which is the hypothesis of the theory of Plasticity.

As the resolution increases by one order of magnitude (3.04 pixels/ μm^2), the fractal dimension decreases, dropping to values ranging between 1.20 and 1.55. This is due to the transition from a fully developed web of microcracks in the matrix to the local properties of isolated microcracks (Fig. 9b, e). Nevertheless, damage patterns maintain self-similar character in a wide range of the scaling regime. At very high resolutions (30.4 pixels/ μm^2) the width of the cracks is very large and the subsequent image-processing may lead to anomalous thinned crack patterns (Fig. 9c, f). Also, very low fractal dimensions are provided. It was thus decided to skip the highest-resolution images from the fractal analysis.

If the complex character of the energy dissipation taking place at the crack boundaries is investigated, the local fractal dimension of the crack lips has to be measured (as in the case of tensile profiles), instead of the damage dimension Δ_d of the entire 2D net-

work. For this purpose, a different technique proved to be more effective in the binary thinning of the thresholded images (Vervuurt et al., 1995). Instead of averaging white pixels (corresponding to the Wood's metal) through the width (skeletonizing process, Fig. 10b), binary thinning can be performed by isolating the boundaries of the cracks (Fig. 10c). The box-counting analysis on the crack lips reveals self-affine scaling at the local level, and yields values of the fractal dimension very close to those of the tensile fracture profiles.

5. Conclusions: Consequences of fractality

The experimental determination of the fractal properties of any real set has to tackle with the inherent discreteness of the digitized data. Care must be taken when evaluating the results, especially if multifractal domains are considered. Any data acquisition technique provides an extrinsic characteristic size which is superposed to the intrinsic length of the domain. Thus, a lower cut-off in the scaling regime has to be clearly defined. The representative range of fractality has to be individuated for any material.

The invasive fractal character of the fracture patterns in concrete has been fully confirmed by the experimental investigations. Thereby, fracture energy is dissipated inside complex fractal spaces and should be considered intermediate between surface energy (LEFM) and volumetric energy (theory of Plasticity,

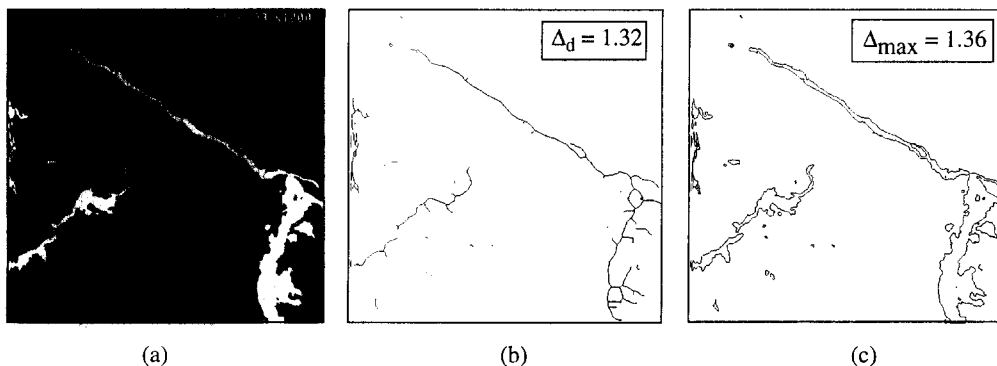


Fig. 10. Binary thinning of a thresholded image (a): averaging (b) through the width (skeletonizing), and outlining the boundaries of the cracks (c).

Damage mechanics). Stress-induced cracking possesses *self-similar* scaling properties when the global damage network is considered. This represents a piece of evidence of the multiscale self-organization of energy dissipation in the bulk of heterogeneous materials. When the lips of a single propagating crack are considered, both in tension and compression, *self-affine* scaling comes into play, leading to multifractal behavior. In this case, Brownian disorder (characterized by a +1/2 dimensional increment) represents the theoretical limit for microscopic complexity. In any case, further investigation is required to confirm this assertion.

From a fracture mechanics point of view, fractality permits to explain the *stable crack growth* occurring in the first stages of crack propagation. This behavior is physically related to the smoothing of the stress-singularity at the crack tip (Carpinteri and Chiaia, 1995b). The invasive fractality provides an attenuation of the fracture localization, involving an attenuation of the stress singularity and, macroscopically, a more ductile behavior of disordered materials. By extending the well-known Griffith criterion for brittle fracture to the case of fractal cracks, Carpinteri and Chiaia (1995b) obtained a new toughness parameter, namely the *fractal stress intensity factor*, which presents the following anomalous physical dimensions:

$$[K_I^*] = [F][L]^{-(3+d_{\mathcal{F}})/2}. \quad (2)$$

Generalizing Irwin's solution, the following near-tip elastic stress field can be obtained, where $d_{\mathcal{F}}$ is the fractional dimensional increment of the fracture domain with respect to the canonical surface dimension:

$$\sigma_{ij} = K_I^* r^{-(1-d_{\mathcal{F}})/2} f_{ij}(\theta). \quad (3)$$

When $d_{\mathcal{F}} = 0$ ($\Delta = 2$) we have the classical relations of LEFM (stress singularity $\approx r^{-1/2}$). When $d_{\mathcal{F}} = 1$, as a limit case, we find that the stress-singularity at the crack tip vanishes and no localization occurs, as if the energy were dissipated in the volume ($\Delta = 3$).

The above theory naturally yields *R-curve* behavior. While in the case of smooth cracks the *crack-resistance* is independent of crack length a , in the presence of fractal cracks it increases with a , following a power-law with exponent equal to the fractal

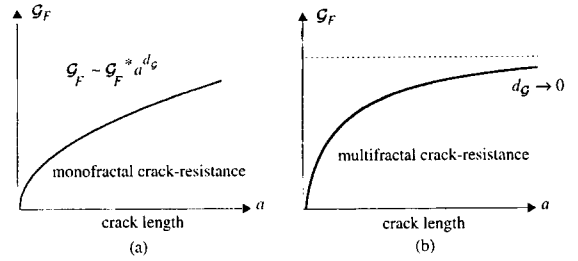


Fig. 11. Stable crack growth according to a monofractal (a) and to a multifractal (b) *R-curve* behavior.

dimensional increment $d_{\mathcal{F}}$ (Fig. 11a). Moreover, since the fractal increment $d_{\mathcal{F}}$ progressively tends to zero as the damage spreads (Fig. 5), a *plateau* in the crack-resistance curve is always detected (Fig. 11b). The dimensional transition of the dynamical stress-intensity factor is also responsible for the slower speed of crack propagation with respect to the theoretical Raleigh speed.

From a structural point of view, the positive size-scale effect on the values of the nominal toughness (K_{IC} or \mathcal{G}_F) of real structures can be adequately explained by the complexity of energy dissipation occurring, at the material level, in fractal spaces. Carpinteri (1994) demonstrated that, if b is a reference size of the structure, the nominal fracture energy \mathcal{G}_F ($[F][L]^{-1}$) increases with size by following a slope equal to $d_{\mathcal{F}}$ in the bilogarithmic diagram $\log \mathcal{G}_F$ vs. $\log b$ (Fig. 12a). By considering a monofractal domain ($d_{\mathcal{F}} = \text{constant}$), an infinite value of fracture energy would be provided for the larger sizes, which is not corresponding to reality. Therefore, taking into account the multifractality of the fracture domains, a multifractal scaling law (MFSL) for the nominal fracture energy \mathcal{G}_F has been proposed by Carpinteri and Chiaia (1996). The analytical expression for the multifractal scaling law, represented in Fig. 12b, is the following:

$$\mathcal{G}_F(b) = \mathcal{G}_F^\infty \left[1 + \frac{l_{ch}}{b} \right]^{-1/2}, \quad (4)$$

where \mathcal{G}_F^∞ is the nominal asymptotic fracture energy, valid in the limit of infinite structural size ($b \rightarrow \infty$), and l_{ch} is the value of a characteristic internal length, which controls the transition from the fractal regime

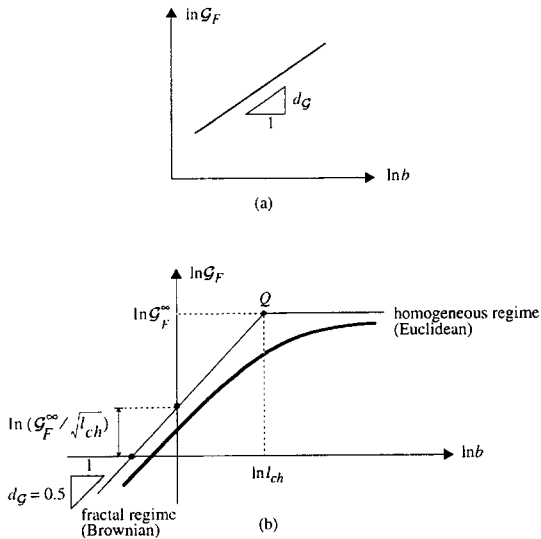


Fig. 12. Size effects on concrete fracture energy. Monofractal (a) and multifractal (b) scaling laws.

to the euclidean one. On the basis of the MFSL, the nominal fracture energy appears to be a physically meaningful parameter only in the homogeneous regime, that is, for large specimens. From an engineering point of view, the MFSL allows for the extrapolation from laboratory-sized specimens to a reliable value of the fracture energy valid for real-sized concrete structures. The MFSL was thus successfully applied to various experimental data (Carpinteri and Chiaia, 1996).

Acknowledgements

The present research was carried out with the financial support of the Italian Ministry of University and Scientific Research (MURST) and of the National Research Council (CNR). Support of the University of California at Berkeley is also gratefully acknowledged.

References

- Carpinteri, A., 1989. Cusp catastrophe interpretation of fracture instability. *J. Mech. Phys. Solids* 37, 567–582.
- Carpinteri, A., 1994. Fractal nature of material microstructure and size effects on apparent mechanical properties. *Mech. Mater.* 18, 89–101.
- Carpinteri, A., Chiaia, B., 1995a. Multifractal nature of concrete fracture surfaces and size effects on nominal fracture energy. *Mater. Struct.* 28, 435–443.
- Carpinteri, A., Chiaia, B., 1995b. Crack-resistance behavior as a consequence of self-similar fracture topologies. *Int. J. Fract.* 76, 327–340.
- Carpinteri, A., Chiaia, B., 1996. Size effects on concrete fracture energy: Dimensional transition from order to disorder. *Mater. Struct.* 29, 259–266.
- Chudnowski, A., Kunin, B., 1987. A probabilistic model of brittle crack formation. *J. Appl. Phys.* 62, 4124–4133.
- El Naschie, M.S., 1996. Kolmogorov turbulence, Apollonian fractals and the Cantorian model of Quantum space-time. *Chaos Solitons Fractals* 7, 147–149.
- Hillerborg, A., Modeer, M., Petersson, P.E., 1976. Analysis of crack formation and crack growth in concrete by means of fracture mechanics and finite elements. *Cement Concrete Res.* 6, 773–782.
- Mandelbrot, B.B., 1982. *The Fractal Geometry of Nature*, W.H. Freeman and Company, New York.
- Mandelbrot, B.B., 1985. Self-affine fractals and fractal dimension. *Phys. Scr.* 32, 257–260.
- Myer, L.R., Kemeny, J.M., Zheng, Z., Suarez, R., Ewy, R.T., Cook, N.G.W., 1992. Extensile cracking in porous rock under differential compressive stress. *Appl. Mech. Rev.* 45, 263–280.
- Nemat-Nasser, S., Hori, M., 1993. *Micromechanics: Overall properties of heterogeneous materials*, North-Holland, Amsterdam.
- Nemati, K.M., 1994. Generation and interaction of compressive stress-induced microcracks in concrete, Ph.D. Thesis, Department of Civil Engineering, University of California at Berkeley.
- Scrivener, K.L., Nemati, K.M., 1996. The percolation of pore space in the cement paste/aggregate interfacial zone of concrete. *Cement Concrete Res.* 26, 35–40.
- Vervuurt, A., Chiaia, B., Van Mier, J.G.M., 1995. Damage evolution in different types of concrete. *Heron* 40, 285–311.
- Vonk, R.A., 1993. A micromechanical investigation of softening of concrete loaded in compression. *Heron* 38, 1–94.
- Zheng, Z., Cook, N.G.W., Doyle, F.M., Myer, L.R., 1988. Preservation of stress-induced microstructures in rock specimens, Report, Lawrence Berkeley Laboratory, University of California, Berkeley, pp. 1–14.